AFRL-AFOSR-UK-TR-2022-0013

Broadband Scanning Microwave Microscopy of Phosphorene

Farina, Marco
UNIVERSITA' POLITECNICA DELLE MARCHE
PIAZZA ROMA 22
ANCONA, ANCONA, 60121
ITA

01/11/2022
Final Technical Report

DISTRIBUTION A: Distribution approved for public release.

Air Force Research Laboratory
Air Force Office of Scientific Research
European Office of Aerospace Research and Development
Unit 4515 Box 14, APO AE 09421

REPORT DOCUMENTATION PAGE

PLEASE DO NOT RETURN YOUR FORM TO THE ABOVE ORGANIZATION.

1. REPORT DATE	2. REPORT TYPE	3. DATES COVERED START DATE	3. DATES COVERED END DATE
20220111	Final	20170930	20210929

4. TITLE AND SUBTITLE
Broadband Scanning Microwave Microscopy of Phosphorene

5a. CONTRACT NUMBER	5b. GRANT NUMBER	5c. PROGRAM ELEMENT NUMBER
	FA9550-17-1-0043	61102F
5d. PROJECT NUMBER	**5e. TASK NUMBER**	**5f. WORK UNIT NUMBER**

6. AUTHOR(S)
Marco Farina

7. PERFORMING ORGANIZATION NAME(S) AND ADDRESS(ES)
UNIVERSITA' POLITECNICA DELLE MARCHE
PIAZZA ROMA 22
ANCONA, ANCONA 60121
ITA

8. PERFORMING ORGANIZATION REPORT NUMBER

9. SPONSORING/MONITORING AGENCY NAME(S) AND ADDRESS(ES)	10. SPONSOR/MONITOR'S ACRONYM(S)	11. SPONSOR/MONITOR'S REPORT NUMBER(S)
EOARD UNIT 4515 APO AE 09421-4515	AFRL/AFOSR IOE	AFRL-AFOSR-UK-TR-2022-0013

12. DISTRIBUTION/AVAILABILITY STATEMENT
A Distribution Unlimited: PB Public Release

13. SUPPLEMENTARY NOTES

14. ABSTRACT
This research project aims to develop a broadband scanning microwave microscope (SMM) for the characterization of the electromagnetic properties of 2D atomic-layered materials. The work was carried out through a close collaboration between the PI at the Marche Polytechnical University in Italy and the co-PI at Lehigh University and Cornell University. The main technical accomplishments through the past four years included examinations of biological and semiconductor specimens. As shown in the Final Progress Report, many papers were published.

15. SUBJECT TERMS

16. SECURITY CLASSIFICATION OF: a. REPORT	b. ABSTRACT	c. THIS PAGE	17. LIMITATION OF ABSTRACT	18. NUMBER OF PAGES
U	U	U	SAR	13

19a. NAME OF RESPONSIBLE PERSON	19b. PHONE NUMBER *(Include area code)*
KENNETH GORETTA	426-7349

FINAL TECHNICAL REPORT
U.S.A.F. Office of Scientific Research Grant No. FA9550-17-1-0043
"Broadband Scanning Microwave Microscopy of Phosphorene"

PI: Professor Marco Farina
Department of Information Science
Marche Polytechnical University, Ancona, Italy 60131
Tel: +39 (071) 2204837
Email: m.farina@univpm.it

Co-PI: Professor James C. M. Hwang
Department of Materials Science and Engineering
Cornell University, Ithaca NY 14853-1501
Email: jch263@cornell.edu

Period of Performance: from 09.30.2017 to 12.28.2021

Summary

This research project aims to develop a broadband scanning microwave microscope (SMM) for the characterization of the electromagnetic properties of 2D atomic-layered materials. The work was carried out through a close collaboration between the PI at the Marche Polytechnical University in Italy and the co-PI at Lehigh University (later Cornell University after the co-PI moved from Lehigh to Cornell) in the US. Experiments were conducted using both SMMs at Marche and Lehigh (Cornell). In-person visits, virtual meetings, and impromptu email and phone discussions occurred regularly between the two groups.

The main technical accomplishments through the past four years include:

1. Refined the SMM for imaging and quantitative characterization of 2D materials.
2. Invented an inverted SMM (iSMM) to improve its bandwidth, sensitivity, and dynamic range.
3. Developed a protocol to remove topography crosstalk from the SMM signal.

These results are described in the next three main sections. All referred publications related to the project are listed at the end.

DISTRIBUTION A: Distribution approved for public release. Distribution unlimited

Table of Contents

Summary 1
List of Figures 2
List of Symbols, Abbreviations and Acronyms 3
Introduction 4
Refinement of the SMM for Imaging and Quantitative Characterization of 2D Materials and Structures 4
Invention of an Inverted SMM 8
Real-Time Removal of Topography Crosstalk 9
Conclusion 11
Refereed Publications 12

List of Figures

Fig. 1. (a) Flat 2DEG, (b) patterned 2DEG, and (c) patterned 2DHG heterostructures. 5
Fig. 2. (a) AFM topography image, (b) SMM conductance/capacitance contrasts, (c) SMM conductance image, and (d) SMM capacitance image of a flat 2DEG heterostructure [Fig. 1(a)]. Dashed curves are simulated. .... **Errore. Il segnalibro non è definito.**
Fig. 3. (a) AFM topography image, (b) SMM conductance/capacitance contrasts, (c) SMM conductance image, and (d) SMM capacitance image of a patterned 2DEG heterostructure [Fig. 1(b)]. Dashed curves are simulated. 6
Fig.4. (a) AFM topography image, (b) SMM conductance/capacitance contrasts, (c) SMM conductance image, and (d) SMM capacitance image of a patterned 2DHG heterostructure [Fig. 1(c)]. Dashed curves are simulated...7
Fig. 5. (a) Schematics and (b) 2-port equivalent circuit of an inverted scanning microwave microscope.. .... **Errore. Il segnalibro non è definito.**
Fig. 6. iSMM $PtSe_2$ images of (a) Re(Y) and (b) Im(Y)/ω, with surrounding gold appearing in blue. (c) and (d) are line scans of (a) and (b), respectively. Dotted curves are smoothed trends.............9
Fig. 7. Measured (green dot) vs. simulated (curves) Re(Y) as a function of $PtSe_2$ conductivity. Inset shows details around 10^3 S/m.. 10
Fig. 8. (a) AFM h^* image, SMM $\angle S_{11}^*$ image, and linear scans across the dashed lines on the images. (b) topography-corrected $\angle S_{11}^* - h^*$ image, AFM PFM image, and linear scans across the dashed lines on the images.. .... **Errore. Il segnalibro non è definito.**

DISTRIBUTION A: Distribution approved for public release. Distribution unlimited

List of Symbols, Abbreviations and Acronyms

$\angle S_{11}^*$: normalized phase of the reflection coefficient
$\Delta \boldsymbol{S}$: scattering matrix variation
$\Delta \boldsymbol{S}^*$: normalized scattering matrix variation
φ: half cone angle of probe
σ: electrical conductivity
2D: two dimensional
2DEG: two-dimensional electron gas
2DHG: two-dimensional hole gas
AFM: atomic force microscopy
AlN: aluminum Nitride
Al_2O_3: aluminum oxide
AlGaN: aluminum gallium nitride
BCl_3: boron trichloride
C_{BALL}: capacitance of probe tip
C_{CANTI}: capacitance of probe cantilever
C_{CONE}: capacitance of probe cone
Co-PI: co-principal investigator
dB: decibel
G: ground line
GaN: gallium nitride
h: sample topography
h^*: normalized sample topography
H: probe body length
HfZrO: hafnium zirconium oxide
InAlN: indium aluminum nitride
iSMM: inverted scanning microwave microscope
PFM: piezoelectric force microscopy
PI: principal investigator
P_{in}: input power
P_{out}: output power
Pt: platinum
$PtSe_2$: platinum diselenide
r: probe tip radius
$\boldsymbol{S}$: scattering matrix
S_{11}: reflection coefficient
S_{21}: transmission coefficient
Si: silicon
SiC: silicon carbide
SiO_2: silicon dioxide
SL: signal line
SMM: scanning microwave microscopy
SNOM: scanning near-field optical microscope
STM: scanning tunneling microscope
VNA: vector network analyzer
Y: probe-sample interaction admittance

DISTRIBUTION A: Distribution approved for public release. Distribution unlimited

Introduction

The project was planned for phosphorene, but switched to platinum diselenide ($PtSe_2$), because monolayer $PtSe_2$ features a sizable bandgap, high carrier mobility, air stability, and can be synthesized in large areas. With the approval of Drs. Jason Foley and Dr. Kenneth Goretta of AFOSR, the scope of the project was expanded to include other promising 2D materials such as $PtSe_2$. Besides $PtSe_2$, we have also analyzed and characterized 2D electron and hole gases (2DEG and 2DHG) buried at the interface of AlN/GaN heterostructures. The methodology developed can be extended to many other 2D systems.

A major accomplishment in the project is the invention of an inverted scanning microwave microscope (iSMM). This new technique allows any existing scanning probe microscope such as an atomic force microscope (AFM), a scanning tunneling microscope (STM), or a scanning near-field optical microscope (SNOM), to be converted into an SMM with a simple modification of the sample holder. For example, different iSMMs were developed based on the Keysight SMM at Lehigh (Cornell) and the NT-MDT SMM at Marche. The iSMM exhibited better bandwidth, sensitivity, and dynamic range than traditional SMMs do. A calibration procedure was developed for the iSMM and used for quantitative characterization of $PtSe_2$.

The topography crosstalk has been extensively analyzed. This is an artifact caused by the vertical movement of the SMM probe as it traces the sample surface. The movement changes the parasitic impedance of the probe even for a sample with uniform electromagnetic properties. This masks the intrinsic electromagnetic properties of the sample. Therefore, we developed an efficient technique to remove the topography crosstalk and to extract the intrinsic electromagnetic properties in real time. The technique is applicable to a wide range of materials and devices, including 2D materials and semiconductor heterostructures.

Refinement of the SMM for Imaging and Quantitative Characterization of 2D Materials and Structures

The Lehigh (Cornell) SMM was modified to enable broadband sweep up to 20 GHz instead of a single frequency. The obtained SMM results confirmed the benefit of broadband SMM with improved sensitivity and image quality especially after time-gated postprocessing of data. Using the topography information simultaneously obtained by the AFM and the *in situ* extracted probe geometry, we de-embed from the topography-corrupted SMM data the sheet resistance of 2D electron or hole gas (2DEG or 2DHG) buried at the interface of an AlN/GaN heterostructure, including the lateral depletion of the 2DEG from an etched step. The SMM results are validated by Hall-effect measurements. With an improved setup, the SMM can be used to nondestructively monitor the sheet resistance of 2DEG or 2DHG during device manufacture. These studies help pave the way to 3D microwave tomography on the nanometer scale of multilayer structures.

Fig. 1 illustrates schematically the three types of AlN/GaN heterostructures used: (a) a flat 2DEG heterostructure, (b) a patterned 2DEG heterostructure, and (c) a patterned 2DHG heterostructure. As part of device fabrication, the active regions of 2DEG and 2DHG are isolated by selective-area ion bombardment or BCl_3-based plasma etching. The former results in a flat surface; the latter results in steps of 39 nm and 200 nm on the 2DEG and 2DHG heterostructures, respectively. Both

DISTRIBUTION A: Distribution approved for public release. Distribution unlimited

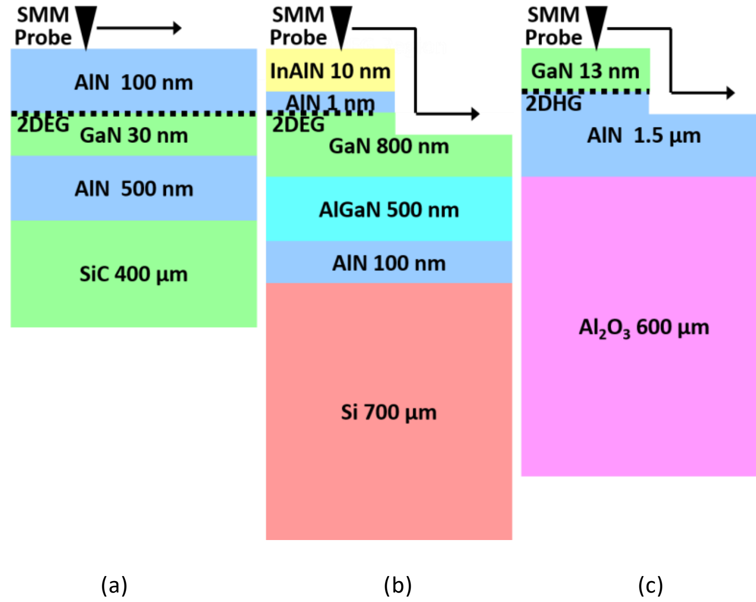

Fig. 1. (a) Flat 2DEG, (b) patterned 2DEG, and (c) patterned 2DHG heterostructures.

flat and patterned heterostructures are scanned at 6.2 GHz, a tradeoff between sensitivity and signal-to-noise ratio. The reflection coefficient S_{11} is calibrated by modeling the probe geometry with a half ball attached to a truncated cone, which is in turn attached to a cantilever. The slender cone minimizes the cantilever capacitance.

It is commonly assumed that the topography crosstalk on the total interaction capacitance, including that of the ball (C_{BALL}), cone (C_{CONE}), and cantilever (C_{CANTI}), is a function of the probe height z only. This allows the topography crosstalk to be corrected by the z values measured by the AFM. However, when the topographic feature size (e.g., step height) approaches the probe size (r), C_{BALL} and C_{CONE} can also be functions of the lateral distances x and y from the feature. Therefore, in this work, we use 3D COMSOL to simulate the topography crosstalk on C_{BALL} and C_{CONE} as the probe scans across an active region of 2DEG or 2DHG. The topography crosstalk on C_{CANTI} is neglected because it is estimated to be on the order of 0.01 fF, much smaller than the total capacitance contrast induced by the 2DEG or 2DHG as shown in Fig. 2, Fig. 3, and Fig. 4. These figures also show agreement between simulation and measurement.

Fig. 2 shows the AFM topography image and SMM interaction conductance and capacitance images for the flat 2DEG heterostructure [Fig. 1(a)]. It can be seen in Fig. 2(a) that the AFM image is featureless except for randomly distributed atomic steps of 0.3 nm. By contrast, the 2DEG region is distinguishable in the SMM images having average conductance contrast of 0.47 ± 0.30 µS and capacitance contrast of 0.18 ± 0.03 fF with respective to the isolated region and consistent with that simulated as illustrated in Fig. 2(b). However, the conductance contrast can narrow down the range of the 2DEG sheet resistance to 960 ± 840 Ω/□, in general agreement with the Hall-measured value of 450 Ω/□.

Fig. 3 shows that the active region of the patterned 2DEG heterostructure [Fig. 1(b)] is distinguishable in not only the SMM conductance/capacitance images, but also the AFM topography image as expected. Comparing the measured and simulated conductance/capacitance

DISTRIBUTION A: Distribution approved for public release. Distribution unlimited

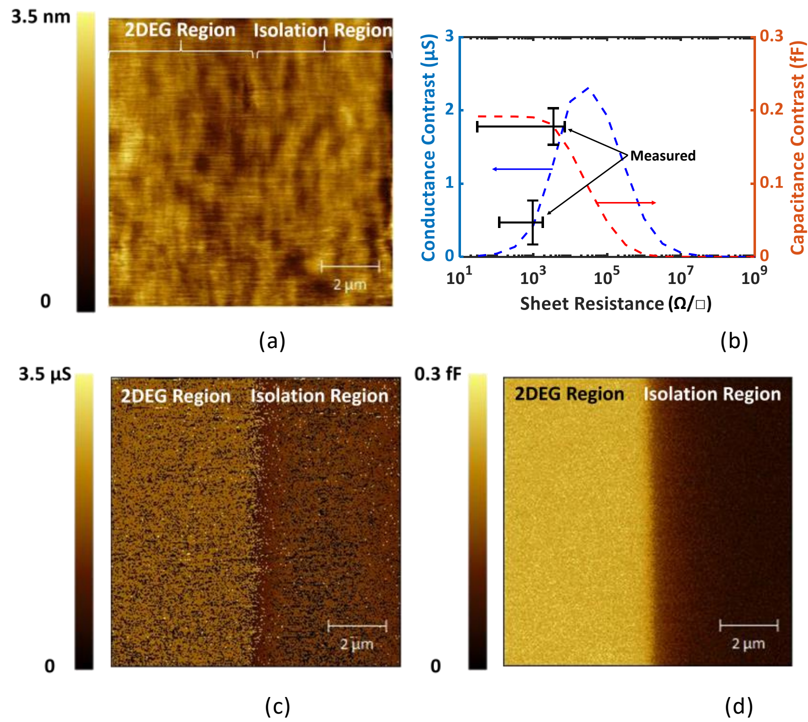

Fig. 2. (a) AFM topography image, (b) SMM conductance/capacitance contrasts, (c) SMM conductance image, and (d) SMM capacitance image of a flat 2DEG heterostructure [Fig. 1(a)]. Dashed curves are simulated.

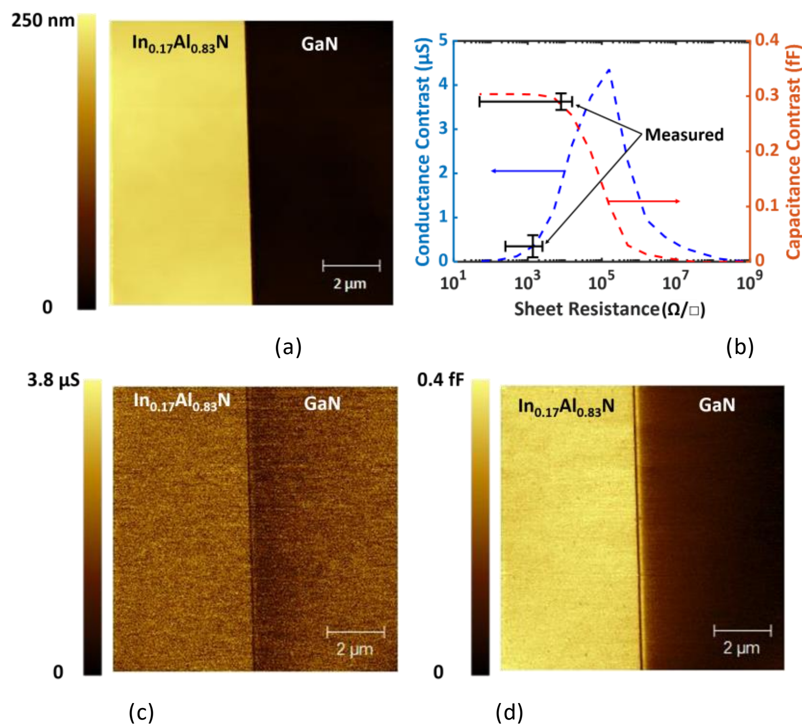

Fig. 3. (a) AFM topography image, (b) SMM conductance/capacitance contrasts, (c) SMM conductance image, and (d) SMM capacitance image of a patterned 2DEG heterostructure [Fig. 1(b)]. Dashed curves are simulated.

DISTRIBUTION A: Distribution approved for public release. Distribution unlimited

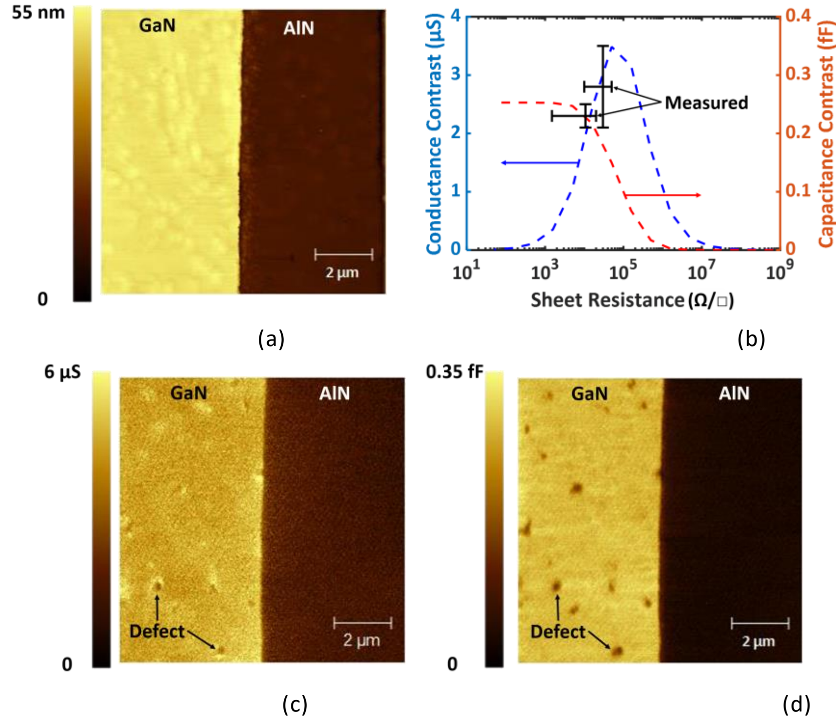

Fig. 4. (a) AFM topography image, (b) SMM conductance/capacitance contrasts, (c) SMM conductance image, and (d) SMM capacitance image of a patterned 2DHG heterostructure [Fig. 1(c)]. Dashed curves are simulated.

contrasts, the conductance contrast can again narrow down the 2DEG sheet resistance range to 1.4 ± 1.1 kΩ/□, which is higher than the Hall-measured value of 200 Ω/□. The difference may be due to the Schottky barrier between the SMM probe and $In_{0.17}Al_{0.83}N$, which partially depletes the 2DEG. Upon close examination, it can be seen that the contrast between $In_{0.17}Al_{0.83}N$ and GaN is sharp in the AFM image, but an extra fringe beyond the edge is present in the SMM images. The extra SMM fringe can be explained by the finite SMM probe size compared to the step height. When the probe starts to roll off the edge, its overlap with the 2DEG decreases and so does the interaction capacitance. However, when the probe just lands on GaN, its side contacts the 2DEG edge, resulting in a local peak in the capacitance and an extra fringe in the image. The height of this peak and the depth of the valley before the peak may be modulated by the 2DEG depletion width d from the edge. Comparing the simulated and measured data, it is estimated that $d \approx 0.2$ µm. This shows that SMM can be used to quantify not only the sheet resistance of the 2DEG, but also the depletion width of the 2DEG from the etched step. The depletion width may result from both the Scottky barrier and the free surface, so their effects need to be separated by a more detailed analysis.

Similar to Fig. 3, Fig. 4 shows that the active region of the patterned 2DHG heterostructure [Fig. 1(c)] is distinguishable in not only the SMM conductance/capacitance images, but also the AFM topography image. As the probe scans from the GaN mesa down to the AlN region, the average contrast is 39 ± 2 nm in topography, 2.8 ± 0.7 µS in conductance, and 0.23 ± 0.02 fF in capacitance. It can be seen that the higher sheet resistance of the 2DHG makes it more sensitive to the SMM conductance contrast, so that it is more accurately determined to be 13 ± 5 kΩ/□, which agrees with the 15 kΩ/□ value of the Hall measurement. Compared to Fig. 3, the SMM images of the 2DHG do not show any extra fringe near the etched step, probably because the step height of 39

DISTRIBUTION A: Distribution approved for public release. Distribution unlimited

nm is much smaller than the probe radius. On the other hand, the SMM images show defect spots that are absent in the AFM image. These defects appear darker, indicating higher resistance than the surrounding 2DHG. The defect density is approximately 3×10^7 cm^{-2}, which is orders-of-magnitude lower than the typical threading dislocation density in AlN and GaN layers grown on foreign substrates such as Si, SiC, and Al_2O_3. This suggests that not all dislocations are electrically active. The nature of these defects needs to be better characterized, because they can be scattering centers for mobile holes.

Invention of an Inverted SMM

Traditionally, an SMM is modified from an AFM or a scanning tunneling microscope (STM), so that the probe can be scanned at a fixed height (0–1 nm) above the sample through the feedback control of atomic force or tunneling current. In either case, the microwave signal is injected through the probe by a vector network analyzer (VNA), and the signal reflected from the sample is also sensed by the VNA. Such a one-port reflection measurement usually has a dynamic range of 40–60 dB as limited by directional couplers.

To minimize the parasitic interaction and to boost the SMM sensitivity without resorting to a resonance circuit, we invented the iSMM. As shown schematically in Fig. 5(a), in an iSMM, the scanning probe is always grounded and the microwave signal is injected through a transmission line (e.g., a slot line, a coplanar waveguide, or a microstrip line) as part of the sample holder. Unlike the traditional SMM probe, the transmission line can have a broadband impedance match over many decades of frequency. The input and output of the transmission line are connected to the VNA, so that both reflection and transmission coefficients (S_{11} and S_{21}) are measured. Such a two-port measurement usually has a dynamic range of 120–140 dB, making it easier to sense the perturbance when the probe scans across the sample.

With the microwave signal injected through the sample and the probe grounded, the parasitic interaction between the probe body and the surround is greatly reduced, because most of the surround is grounded in any case. Thus, compared to a traditional SMM, an iSMM can have wider dynamic range, higher sensitivity, and broader bandwidth (by making a resonance circuit unnecessary). Additionally, the probe can be a simple, rugged, and bio-compatible metal stylus. Meanwhile, whether the iSMM is modified from an AFM or STM, the original AFM or STM function is intact so that an iSMM image can be obtained simultaneously with an AFM or STM image.

For both SMM and iSMM, the intrinsic interaction between the probe and the sample can be represented by an admittance Y. The equivalent circuit of the iSMM is well defined as shown in Fig. 5(b) in which ABCD matrices represent the error networks related to cables, connectors, etc.

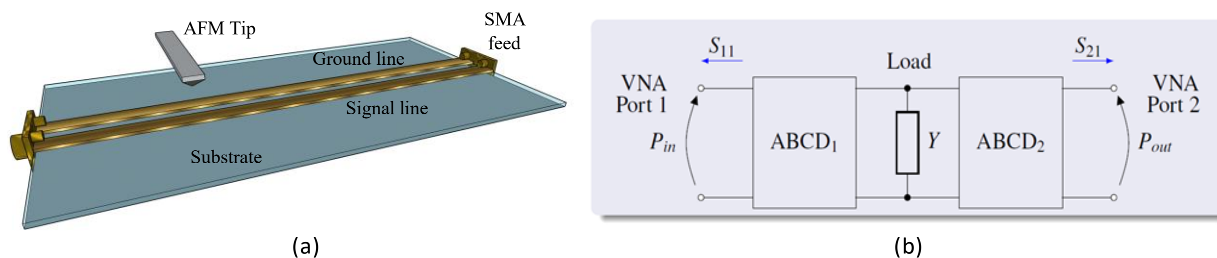

Fig. 5. (a) Schematics and (b) 2-port equivalent circuit of an inverted scanning microwave microscope.

DISTRIBUTION A: Distribution approved for public release. Distribution unlimited

Starting from the ABCD matrices, calibration of reflection and transmission parameters have been developed to de-embed *Y* from the measured data and to extract the intrinsic sample parameters. This calibration method has been validated through numerical simulations.

The iSMM was used to characterize exfoliated $PtSe_2$ flakes that were transferred onto an iSMM sample holder. $PtSe_2$ was selenized at 400 °C from Pt sputtered onto Si. It was then transferred by an adhesive tape to the iSMM holder. The transfer resulted in flakes of multi-layer $PtSe_2$ with properties similar to those of bulk $PtSe_2$.

With proper calibration, the intrinsic probe-sample admittance *Y* is extracted from S_{21} measured at 4.7 GHz on $PtSe_2$ and split into real and imaginary parts as shown in Fig. 6(a) and Fig. 6(b), respectively. Line scans from these figures are plotted in Fig. 6(c) and Fig. 6(d), respectively, to quantify the $PtSe_2$ conductivity. Comparing the measured and simulated real *Y* (Fig. 7), it is estimated that the $PtSe_2$ conductivity is in the range 10^3–10^4 S/m, consistent with the SMM result on 3-nm thick $PtSe_2$. However, it can be seen in Fig. 7 that this range of conductivity is beyond the most sensitive range of the current iSMM.

Real-time Removal of Topography Crosstalk

For the first time, we developed a technique to remove the topography crosstalk in real time during an SMM scan. The technique was proved on a hafnium-zirconium oxide (HfZrO) ferroelectric sample with a rough surface. By removing the topography crosstalk caused by the rough surface, the ferroelectric domain structure is revealed independent of the topography. The

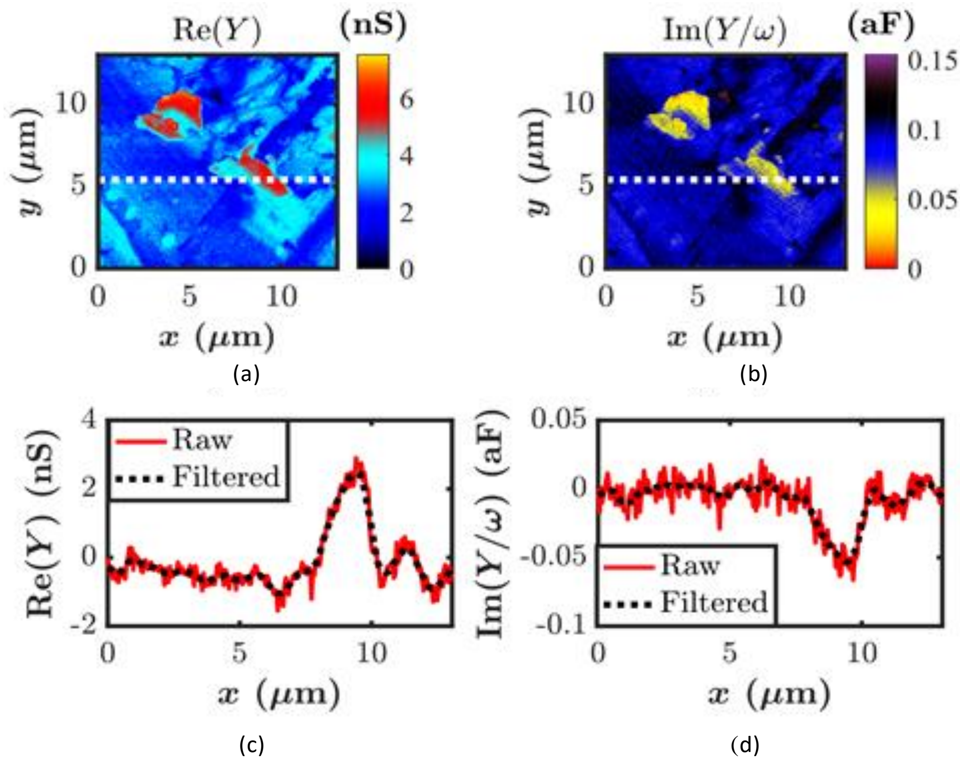

Fig. 6. iSMM $PtSe_2$ images of (a) Re(Y) and (b) Im(Y)/ω, with surrounding gold appearing in blue. (c) and (d) are line scans of (a) and (b), respectively. Dotted curves are smoothed trends.

DISTRIBUTION A: Distribution approved for public release. Distribution unlimited

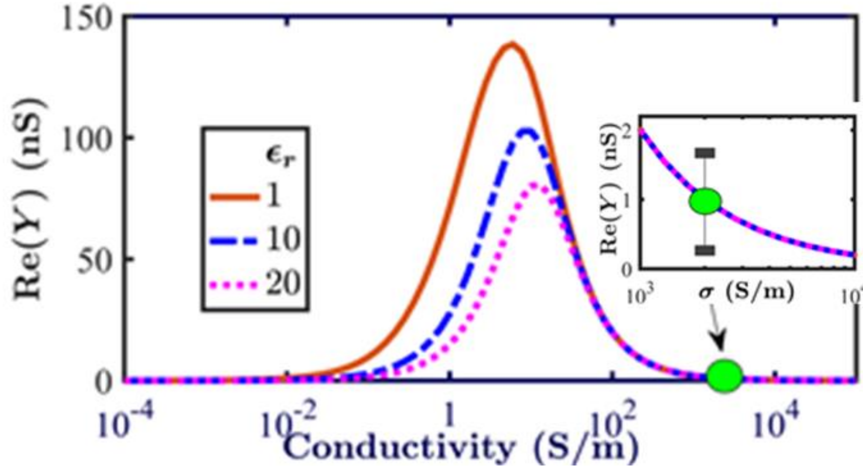

Fig. 7. Measured (green dot) vs. simulated (curves) Re(Y) as a function of $PtSe_2$ conductivity. Inset shows details around 10^3 S/m.

effectiveness of the technique was validated by operating the AFM in the piezoelectric force microscopy (PFM) mode, which is known to be sensitive to ferroelectric domain structure and not the topography.

The SMM signal can be represented by a matrix ***S*** of scattering parameters as sensed by the VNA through the probe. During an SMM scan, small variations of ***S*** reflect changes in both the topography and the electromagnetic properties of the sample. Knowing the topography by the simultaneous AFM scan, the topography crosstalk can be approximated by assuming a linear relationship between the perturbation $\Delta\boldsymbol{S}$ and the topography without laborious 3D finite-element multiscale simulation. This greatly speeds up the removal of the topography crosstalk, making it possible to be done in real time during the SMM scan. Consequently, this provides instant feedback of the scan area and can be used by the operator to zero in on the most interesting area of the sample. The real-time removal of the topography crosstalk includes the following major steps:

1. Acquire simultaneously SMM and AFM signals in terms of $\Delta\boldsymbol{S}$ and h, respectively.
2. Correct $\Delta\boldsymbol{S}$ for the macroscopic tilt of the sample and normalize it between 0 and 1 as $\Delta\boldsymbol{S}^*$.
3. Correct h for the macroscopic tilt of the sample and normalize it between 0 and 1 as h^*.
4. Subtract h^* from $\Delta\boldsymbol{S}^*$.

For proof of concept, the sample is a 6-nm-thick HfZrO layer grown by atomic layer deposition on a $Pt/SiO_2/Si$ substrate. The sample surface roughness is on the order of 1 µm, which reflects mainly the roughness of the substrate. Crosstalk from such a rough topography completely masks the electromagnetic properties of the sample in the SMM image, which mandates the removal of the topography crosstalk. All SMM scans are performed at 4.5 GHz where the reflection coefficient S_{11} reaches a minimum and the signal-to-noise ratio reaches a maximum.

Fig. 8(a) shows that, because of severe topography crosstalk, the SMM *S*-parameter image $\angle S_{11}^*$ resembles the AFM topography image h^*, where $\angle S_{11}^*$ is the normalized reflection coefficient angle and h^* is the normalized topography. Fig. 8(b) shows that, with real-time removal of the topography crosstalk, the $\angle S_{11}^* - h^*$ image resembles the AFM PFM image with ferroelectric

DISTRIBUTION A: Distribution approved for public release. Distribution unlimited

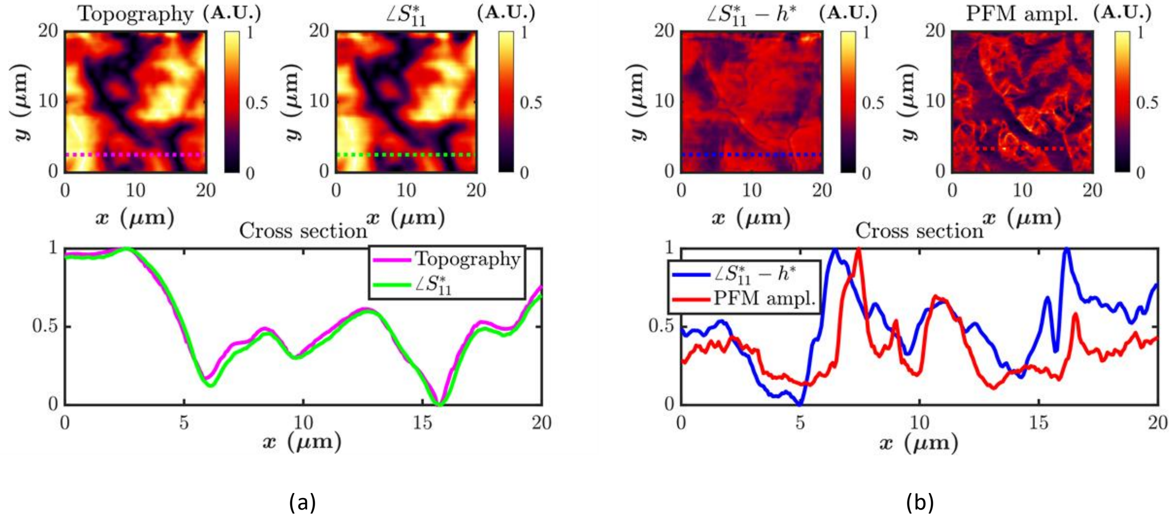

Fig. 8. (a) AFM h^* image, SMM $\angle S_{11}^*$ image, and linear scans across the dashed lines on the images. (b) topography-corrected $\angle S_{11}^* - h^*$ image, AFM PFM image, and linear scans across the dashed lines on the images.

domains delineated. Note that the PFM image is shifted slightly with respect to the SMM image, because, unlike the topography image, it is not simultaneously acquired with the SMM image.

Conclusion

During the project period, different approaches are developed to refine the SMM for the characterization of 2D materials and structures. The main results obtained are:

1. Refinement of the conventional SMM, including improved bandwidth and sensitivity. The improvements are demonstrated on the 2DEG and 2DHG in AlN/GaN heterostructures for the characterization of sheet resistance, depletion width, and high-resistance point defects. The measure sheet resistances are consistent with Hall-measured values, whether the heterostructure is flat or not. Using this approach, the SMM may be used to nondestructively monitor the sheet resistance of low-dimensional materials in actual device structure during fabrication.
2. iSMM, a new variation of the SMM, has been invented with improved sensitivity, bandwidth, ruggedness, and convenience over the traditional SMM. The associated theory and calibration procedure for iSMM has also been developed. All measured results are compared with that simulated by 3D multi-scale full-wave electromagnetic simulations to quantify the conductivity and dielectric constant of the samples. This enables the characterization of the electrical conductivity of $PtSe_2$.
3. A procedure for the fast and effective removal of the topography crosstalk has also been invented, allowing real-time visualization of the electromagnetic properties of the sample in the SMM. The procedure is flexible and easy to use. It does not require any additional measurement besides the sample topography acquired simultaneously by the AFM. It can potentially be applied to a wide variety of samples, including ferroelectric and semiconductor materials.

DISTRIBUTION A: Distribution approved for public release. Distribution unlimited

Refereed Publications

[1] X. Jin, K. Xiong, R. Marstell, N. C. Strandwitz, J. C. M. Hwang, M. Farina, A. Goeritz, M. Wietstruck, and M. Kaynak "Scanning microwave microscopy of aluminum CMOS interconnect lines buried in oxide and water," *European Microwave Conf. (EuMC),* Nuremberg, Germany, Oct. 2017, pp. 975−977.

[2] M. Farina, J. C. M. Hwang, A. Di Donato, E. Pavoni, G. Fabi, A. Morini, F. Piacenza, E, Di Filippo, and T. Pietrangelo, "Imaging of sub-cellular structures and organelles by an STM-assisted scanning microwave microscope at mm-waves," *IEEE MTT-S Int. Microw. Symp. (IMS),* Philadelphia, PA, USA, Jun. 2018, pp. 111–114.

[3] X. Jin, K. Xiong, R. Marstell, N. C. Strandwitz, J. C. M. Hwang, M. Farina, A. Göritz, M. Wietstruck, and M. Kaynak, "Scanning microwave microscopy of buried CMOS interconnect lines with nanometer resolution," *Int. J. Microwave Wireless Technol.,* vol. 10, no. 5/6, pp 556−561, Jun. 2018.

[4] F. Piacenza, A. Biesemeier, M. Farina, F. Piva, X. Jin, E. Pavoni, L. Nisi, M. Cardelli, L. Costarelli, R. Giacconi, A. Basso, E. Pierpaoli, M. Provinciali, J. Hwang, A. Morini, D. Andrea, and M. Malavolta, "Measuring zinc in biological nanovesicles by multiple analytical approaches," *J. Trace Elem. Med. Biol.,* vol. 48, pp. 58–66, Jul. 2018.

[5] M. Farina, X. Jin, G. Fabi, E. Pavoni, A. di Donato, D. Mencarelli, A. Morini, F. Piacenza, R. Al Hadi, Y. Zhao, T. Pietrangelo, X. Cheng, Y. Ning, and J. C. M. Hwang, "Inverted scanning microwave microscope for *in vitro* imaging and characterization of biological cells," *Appl. Phys. Lett.,* vol. 114, no. 9, pp. 093703-1–093703-3, Mar. 2019.

[6] X. Jin, M. Farina, X. Wang, G. Fabi, X. Cheng, and J. C. M. Hwang, "Broadband scanning microwave microscopy of a biological cell with unprecedented image quality and signal-to-noise ratio," *IEEE MTT-S Int. Microw. Symp. (IMS),* Boston, MA, USA, Jun. 2019, pp. 216−219.

[7] G. Fabi, X. Jin, J. C. M. Hwang, C. H. Joseph, E. Pavoni, L. Li, K. Xiong, Y. Ning, D. Mencarelli, A. di Donato, A. Morini, Y. Zhao, R. Al Hadi, and M. Farina, "Inverted scanning microwave microscopy for nanometer scale imaging and characterization of platinum diselenide," *IEEE MTT-S Int. Microw. Symp. (IMS),* Boston, MA, USA, Jun. 2019, pp. 1115−1117.

[8] G. Fabi, J. C. M. Hwang, C. H. Joseph, E. Pavoni, X. Jin, X. Wang, D. Mencarelli, A. di Donato, A. Morini, Y. Zhao, R. Al Hadi, M. Farina, "Nanoscale characterization of biological cells with inverted scanning microwave microscopy," *Nanoinnovation Conf.*, Rome, Italy, Jun. 2019.

[9] E. Pavoni, R. Yivlialin, J. C. Hardly, G. Fabi, D. Mencarelli, L. Pierantoni, G. Bussetti, and M. Farina. "Blisters on graphite surface: A scanning microwave microscopy investigation," *RSC Adv.,* vol. 9, pp. 23156–23160, Jul. 2019.

[10] D. Mencarelli, M. Farina, J. C. M. Hwang *et al.,* "An inverted configuration for scanning microwave microscopy," *Int. Conf. Manipulation, Autom. Rob. Small Scales (MARSS),* Helsinki, Jul. 2019.

[11] X. Jin, M. Farina, X. Wang, G. Fabi, X. Cheng, and J. C. M. Hwang, "Quantitative scanning microwave microscopy of the evolution of a live biological cell in a physiological buffer," *IEEE Trans. Microw. Techn.,* vol. 67, no. 12, pp. 5438–5445, Dec. 2019.

[12] M. Farina and J. C. M. Hwang, "Scanning microwave microscopy for biological applications: Introducing the state of the art and inverted SMM," *IEEE Microw. Mag.*, vol. 21, no. 10, pp. 52–59, Oct. 2020.

[13] G. Fabi, C. H. Joseph, X. Jin, X. Wang, T. Pietrangelo, X. Cheng, J. C. M. Hwang, and M. Farina, "Electrical properties of Jurkat cells: An inverted scanning microwave microscope study," *IEEE MTT-S Int. Microw. Symp. (IMS) Dig.,* Aug. 2020, pp. 238–240.

DISTRIBUTION A: Distribution approved for public release. Distribution unlimited

[14] X. Wang, K. Xiong, L. Li, J. C. M. Hwang, X. Jin, G. Fabi, M. Farina, O. Hartwig, M. Prechtl, G. S. Duesberg, A. Göritz, M. Wietstruck, and M. Kaynak, "Quantitative scanning microwave microscopy of few-layer platinum diselenide," *Eur. Microw. Conf. (EuMC)*, Jaarbeurs Utrecht, Netherlands, Jan. 2021, pp. 987–990.
[15] J. C. M. Hwang, "Label-free noninvasive cell characterization: A methodology using broadband impedance spectroscopy," *IEEE Microw. Mag.,* vol. 22, no. 5, pp. 78–87, May 2021.
[16] G. Fabi, C. H. Joseph, E. Pavoni, X. Wang, R. Al Hadi, J. C. M. Hwang, A. Morini, and M. Farina, "Real-time removal of topographic artefacts in scanning microwave microscopy," *IEEE Trans. Microw. Theory Techn.,* vol. 69, no. 5, pp. 2662–2672, May 2021.
[17] G. Fabi, X. Jin, E. Pavoni, C. H. Joseph, A. Di Donato, D. Mencarelli, X. Wang, R. Al Hadi, A. Morini, J. C. M. Hwang, and M. Farina, "Quantitative characterization of platinum diselenide electrical conductivity with an inverted scanning microwave microscope," *IEEE Trans. Microw. Theory Techn.* vol. 69, no. 7, pp. 3348–3359, Jul. 2021.
[18] C. Ferguson, N. Pini, X. Du, M. Farina, J. M. C. Hwang, T. Pietrangelo, and X. Cheng, "Broadband electrical impedance as a novel characterization of oxidative stress in single L6 skeletal muscle cells," *Anal. Chim. Acta,* vol. 1173, p. 338678, Aug. 2021.
[19] X. Wang, G. Fabi, R. Chaudhuri, A. Hickman, M. J. Asadi, K. Nomoto, H. G. Xing, D. Jena, M. Farina, and J. C. M. Hwang, "Quantitative scanning microwave microscopy of 2D electron and hole gases in AlN/GaN heterostructures," *Appl. Phys. Lett.* Accepted for publication.

DISTRIBUTION A: Distribution approved for public release. Distribution unlimited